Chemical Science

ROYAL SOCIETY OF CHEMISTRY

EDGE ARTICLE

View Article Online
View Journal | View Issue

Cite this: *Chem. Sci.*, 2024, **15**, 1364

All publication charges for this article have been paid for by the Royal Society of Chemistry

Mechanistic insights into radical formation and functionalization in copper/*N*-fluorobenzenesulfonimide radical-relay reactions†

Mukunda Mandal, ‡*[ab] Joshua A. Buss, ‡§[c] Si-Jie Chen, ¶[c] Christopher J. Cramer ||[a] and Shannon S. Stahl *[c]

Copper-catalysed radical-relay reactions that employ *N*-fluorobenzenesulfonimide (NFSI) as the oxidant have emerged as highly effective methods for C(sp^3)–H functionalization. Herein, computational studies are paired with experimental data to investigate a series of key mechanistic features of these reactions, with a focus on issues related to site-selectivity, enantioselectivity, and C–H substrate scope. (1) The full reaction energetics of enantioselective benzylic C–H cyanation are probed, and an adduct between Cu and the *N*-sulfonimidyl radical (•NSI) is implicated as the species that promotes hydrogen-atom transfer (HAT) from the C–H substrate. (2) Benzylic *versus* 3° C–H site-selectivity is compared with different HAT reagents: Cu/•NSI, •O^{t}Bu, and Cl•, and the data provide insights into the high selectivity for benzylic C–H bonds in Cu/NFSI-catalyzed C–H functionalization reactions. (3) The energetics of three radical functionalization pathways are compared, including radical–polar crossover (RPC) to generate a carbocation intermediate, reductive elimination from a formal Cu^{III} organometallic complex, and radical addition to a Cu-bound ligand. The preferred mechanism is shown to depend on the ligands bound to copper. (4) Finally, the energetics of three different pathways that convert benzylic C–H bonds into benzylic cations are compared, including HAT/ET (ET = electron transfer), relevant to the RPC mechanism with Cu/NFSI; hydride transfer, involved in reactions with high-potential quinones; and sequential ET/PT/ET (PT = proton transfer), involved in catalytic photoredox reactions. Collectively, the results provide mechanistic insights that establish a foundation for further advances in radical-relay C–H functionalization reactions.

Received 13th July 2023
Accepted 9th December 2023

DOI: 10.1039/d3sc03597b

rsc.li/chemical-science

Introduction

Methods for selective functionalization of C–H bonds are highly appealing in organic synthesis as they enable streamlined preparation of complex molecules, including pharmaceuticals and agrochemicals.[1–4] Copper-catalyzed radical-relay reactions are emerging as particularly effective methods for C–H functionalization and cross coupling.[5,6] These methods conceptually build on reactions reported by Kharasch and Sosnovsky in the 1950s[7,8] and later mechanistic studies,[9] which introduced a strategy to generate carbon-centered radicals *via* hydrogen-atom transfer (HAT) and functionalization of the radicals with a Cu^{II} species. The Kharasch–Sosnovsky reactions employed peroxide-based oxidants, and subsequent adaptations of these reactions have been used to achieve selective functionalization of benzylic C–H bonds to afford new C–O,[10,11] C–N,[12,13] C–C,[14] and C–F[15] bonds. Analogous reactions, in which the peroxide oxidant is replaced by *N*-fluorobenzenesulfonimide (NFSI), proceed with high C–H site-selectivity, exhibit broad substrate scope, and use the C–H substrate as the limiting reagent (Fig. 1A).[16–28]

Cu catalysts and NFSI appear to be privileged partners in radical-relay reactions with benzylic C–H bonds; however, important mechanistic questions remain unresolved, especially those related to the formation and functionalization of the organic radical. HAT is typically postulated to involve a free N-centered radical (*cf.* Fig. 1A), but alternative reactive species have been recently proposed in which an N-centered radical is

[a]*Department of Chemistry, Chemical Theory Center, and Supercomputing Institute, University of Minnesota, 207 Pleasant Street SE, Minneapolis, MN 55455, USA*

[b]*Max Planck Institute for Polymer Research, Ackermannweg 10, 55128 Mainz, Germany. E-mail: mukunda.chem@gmail.com*

[c]*Department of Chemistry, University of Wisconsin–Madison, 1101 University Avenue, Madison, WI 53706, USA. E-mail: stahl@chem.wisc.edu*

† Electronic supplementary information (ESI) available. CCDC 2239614. For ESI and crystallographic data in CIF or other electronic format see DOI: https://doi.org/10.1039/d3sc03597b

‡ These authors contributed equally to this work.

§ Current address: Department of Chemistry, University of Michigan, Ann Arbor, MI 48109, USA.

¶ Current address: Department of Discovery Chemistry, Merck & Co. Inc., South San Francisco, CA 93080, USA.

‖ Current address: UL Research Institutes, 1603 Orrington St. Suite 2000, Evanston, IL 60201, USA.

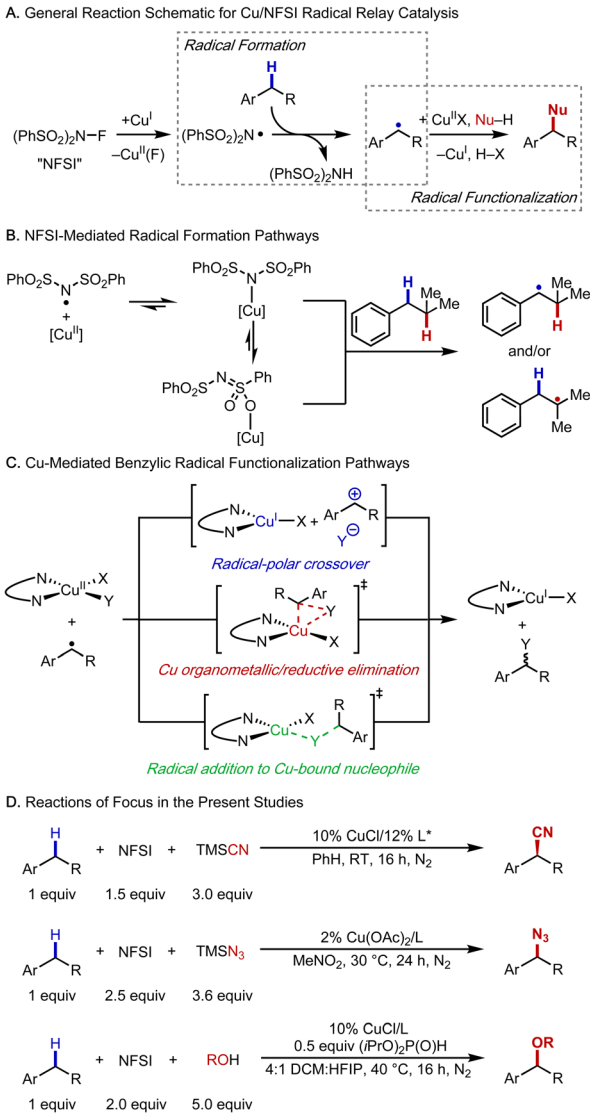

Fig. 1 Mechanistic features of Cu/NFSI-mediated radical-relay reactions. (A) Formation and functionalization of benzylic carbon-centred radicals. (B) The N-centred radical that promotes hydrogen-atom transfer could be coordinated to Cu. (C) Three proposed pathways for functionalization of benzylic radicals. (D) Benzylic C–H cyanation, azidation and etherification provide the basis for the mechanistic investigations in this work.

coordinated to Cu (Fig. 1B).[21] Understanding the nature of the active HAT mediator is important because this species directly influences reaction selectivity.

At least three different pathways have been proposed for functionalization of the organic radical to afford the product (Fig. 1C). These include (1) oxidation of the benzylic radical by Cu^{II} to form a benzylic cation, which can then react with an inner- or outer-sphere nucleophile, corresponding to a radical–polar crossover (RPC) mechanism; (2) radical addition to Cu^{II}, affording a benzylcopper(III) organometallic complex, followed by reductive elimination; and (3) a direct radical addition to a copper-bound nucleophile. Distinguishing among these reaction pathways has implications for enantioselectivity, which has been demonstrated in some cases,[17–19,25] but not in others.[22,27–30]

The present study combines experimental and density functional theory (DFT) investigations to gain insight into the mechanistic features of three Cu/NFSI-mediated benzylic C–H functionalization reactions: cyanation, azidation and methoxylation (Fig. 1D). The complete reaction energetics for enantioselective benzylic cyanation are evaluated, with a focus on the benzylic radical formation and functionalization steps. We find that the N-centered sulfonimidyl radical (˙NSI) forms a thermodynamically favorable adduct with copper(II) that can promote HAT from the benzylic C–H bond. The regioselectivity of HAT by this Cu/˙NSI adduct is compared with that of $^{\cdot}O^{t}Bu$, and ˙Cl, species proposed to serve as the HAT reagent in other C–H functionalization methods. Comparison of experimental and computational data with these three reagents illuminates the unique benzylic site-selectivity evident in Cu/NFSI-mediated reactions. Attention is then given to the radical functionalization step, and the data show that the preferred pathway depends on the identity of the copper species. The nature of the nucleophile and ancillary ligands coordinated to Cu^{II} dictate whether the radical reacts *via* an inner-sphere or an outer-sphere electron-transfer (ET) pathway. The study concludes by comparing radical-relay reactions that involve a radical–polar crossover mechanism (*i.e.*, HAT/ET) with other reactions that feature benzylic cation intermediates: hydride transfer ($H^{-}T$) initiated by 2,3-dichloro-5,6-dicyanobenzoquinone (DDQ)[31] and a multi-step photoredox-initiated pathway involving ET, proton-transfer (PT), and a second ET step (*i.e.*, ET/PT/ET).[32] The data here rationalize why the HAT/ET sequence in the corresponding radical-relay reactions exhibit broader C–H substrate scope relative to reactions involving $H^{-}T$ or ET/PT/ET pathways. Collectively, the results of this study provide a foundation for understanding previously reported reactions and guiding the development of new C–H functionalization methods.

Computational details

All calculations are done employing density functional theory (DFT) as implemented in the Gaussian 16 (Rev. B.01) electronic structure program.[50] The hybrid *meta*-GGA density functional M06 was consistently used throughout the manuscript for our calculations, as it has been successfully applied in a closely related system[21] and has demonstrated reliability in modelling copper-based molecular systems in general.[40a,51] Geometry optimization and frequency calculations are done at the M06-D3(0)/basis-I level of theory,[33,34] where basis-I refers to Ahlrichs' all-electron def2-SVPD basis for all atoms except for the C and H atoms, for which the def2-SVP basis was used.[36] In all cases, an "ultrafine" grid was used for numerical integration in DFT. The natures of all stationary points are verified by calculating quasi-harmonic vibrational frequencies at the same level of theory. Low-frequency vibrational modes below 50 cm^{-1} are replaced with a value of 50 cm^{-1}. For a more accurate estimation of Gibbs free energies (G), single-point electronic energies were re-calculated at the M06-D3(0)/basis-I geometries employing the same DFT functional but using a larger basis set: the def2-TZVPD basis for all atoms except for the C and H atoms, in which case the def2-TZVP basis was used (referred to

as basis-II), and employing the SMD continuum solvation model[35] with solvent parameters for dichloromethane (DCM). This electronic energy, calculated at the M06-D3(0)/basis-II/SMD(DCM) level, was added to thermal contributions to G calculated at the M06-D3(0)/basis-I level to obtain final G values. To account for the standard-state concentration change from 1 atm pressure in the gas phase to 1 M in the solution phase, an entropy "correction" term of 1.89 kcal mol^{-1} was added to the absolute free energies of all computed species. A more detailed discussion regarding this is provided in Section 3 of the ESI.†

For the transition state (TS) structures involving crossing of potential energy surfaces (PES) of different spin multiplicity, *e.g.*, the case of direct transformation of biradical Cu^{II} and the benzyl radical Ar(˙) into singlet Cu^{I} and Ar–X, TSs were located on the broken-symmetry (BS) singlet PES, and the approximate spin-projection scheme of Yamaguchi *et al.*[52] was used for obtaining approximate spin-projected electronic energies of the lower-spin states using eqn (1).

$$E_{AP}^{Singlet} = E^{Triplet} + \frac{2\left(E_{BS}^{Singlet} - E^{Triplet}\right)}{\left\langle \hat{S}^2 \right\rangle^{Triplet} - \left\langle \hat{S}^2 \right\rangle_{BS}^{Singlet}} \quad (1)$$

where, E = electronic energy, BS = broken (spin) symmetry, AP = approximate (spin) projection.

The intrinsic bond orbital (IBO) scheme[39] was used for orbital localization to unravel the mechanistic details of the turnover-limiting hydrogen-atom abstraction step. In this case, wavefunctions at each point along the intrinsic reaction coordinate were obtained at the M06-D3(0)/basis-I level using ORCA 5.0.3. program,[53] and these wavefunctions were then localized to produce the IBOs using the IboView program[54] setting "iboexp = 2".

Results and discussion

Computational analysis of Cu/NFSI-mediated benzylic cyanation

In a recent report, the Liu and Stahl groups disclosed a benzylic cyanation reaction that overcame several historical limitations associated with radical-relay reactions.[17] The reaction employed limiting C–H substrates under mild conditions to afford benzylic cyanation products in high yields and with excellent enantioselectivities across a wide range of substrates, spanning simple building blocks to complex molecules. Preliminary computational analysis was conducted in this work,[17] focusing on the steps associated with functionalization of the radical. Other steps of the reaction were not evaluated. Here, we expand the computational analysis to probe the full reaction energetics (Fig. 2) using DFT at the M06-D3(0)[33,34]/basis-II/SMD(CH_2Cl_2)[35]//M06-D3(0)/basis-I level of theory (see the Computational details section for basis-I and basis-II details). Computations were conducted using a bis(oxazoline)-bound copper(I) chloride pre-catalyst LCu^{I}(Cl), which has been used in each of the three reactions examined in this study (Fig. 1D).

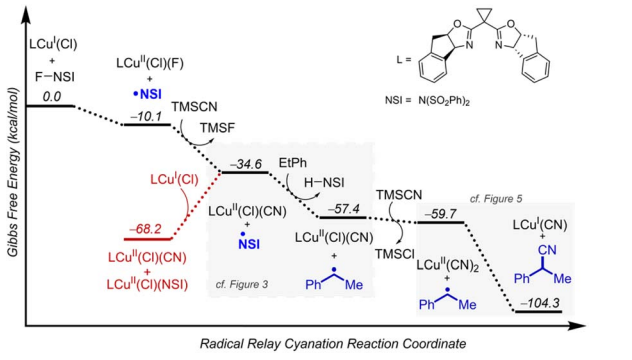

Fig. 2 Full reaction thermodynamics for Cu/NFSI-catalysed benzylic cyanation. Gibbs free energies (kcal mol^{-1}) are computed at M06-D3(0)/basis-II/SMD(CH_2Cl_2)//M06-D3(0)/basis-I level of theory.

The reaction of NFSI with LCu^{I}(Cl) is favourable both kinetically[22,37] and thermodynamically (reaction free energy, $\Delta G^\circ = -10.1$ kcal mol^{-1}, Fig. 2) and affords LCu^{II}(Cl)(F) and the sulfonimidyl radical (˙NSI; Fig. 2).[15,21,22] TMSCN (TMS = trimethylsilyl), employed as the cyanide source in the catalytic reactions, undergoes ligand exchange with LCu^{II}(Cl)(F) to form LCu^{II}(Cl)(CN) in a highly exergonic process ($\Delta G^\circ = -24.5$ kcal mol^{-1}) that is driven by the formation of TMSF, with a strong Si–F bond.[38] Another equivalent of TMSCN can react with LCu^{II}(Cl)(CN) to replace the chloride with another cyanide, generating LCu^{II}(CN)$_2$ in a moderately exergonic process ($\Delta G^\circ = -2.3$ kcal mol^{-1}). Reaction between ˙NSI and a second equivalent of Cu^{I} exhibits high thermodynamic favorability, as shown in Fig. 2 (red). Consequently, the resulting species, LCu^{II}(Cl)(NSI), is anticipated to be present in the reaction equilibrium. In line with this expectation, a structurally analogous L′Cu^{II}(Cl)(NSI) species has been successfully isolated and characterized using X-ray crystallography, where L′ represents a bathophenanthroline ligand (for detailed X-ray crystal structure information, refer to Section 2 of the ESI†). However, this reaction will halt productive reactivity by quenching the active radical and sequestering the copper as a Cu^{II} species that does not promote efficient activation of NFSI (Fig. 2, red).[22] Alternatively, ˙NSI can promote HAT from the benzylic C–H substrate to afford a benzylic radical ($\Delta G^\circ = -22.8$ kcal mol^{-1}). The benzylic radical reacts with LCu^{II}(CN)$_2$ to afford the benzylic nitrile in a highly favorable process ($\Delta G^\circ = -44.6$ kcal mol^{-1}; reaction of the benzylic radical with LCu^{II}(Cl)(CN) is also highly favorable to afford the same cyanation product: $\Delta G^\circ = -40.2$ kcal mol^{-1}).

Formation of the benzylic radical is a crucial step in these reactions, prompting us to give further attention to the active species that promote HAT. In a complementary allylic cyanation reaction with a different N–F reagent, Liu and coworkers proposed that the N-centered radical coordinates to Cu^{II}.[21] Similar behavior was identified here with ˙NSI, which can undergo favorable coordination to LCu^{II}(Cl)(CN) through the sulfonimide nitrogen (κ-N isomer **B**, Fig. 3) or the sulfonyl oxygen atom (κ-O isomer **C**, Fig. 3). Both isomers form closed-shell Cu/NSI adducts (see ESI, Fig. S9† for structural details and Fig. S10† for spin–density plots of the spin-isomers), but the calculations indicate that generation of the κ-O isomer is thermodynamically more favorable ($\Delta G_C^\circ = -8.9$ kcal mol^{-1}) than the κ-N counterpart ($\Delta G_B^\circ = -4.8$ kcal mol^{-1}). The

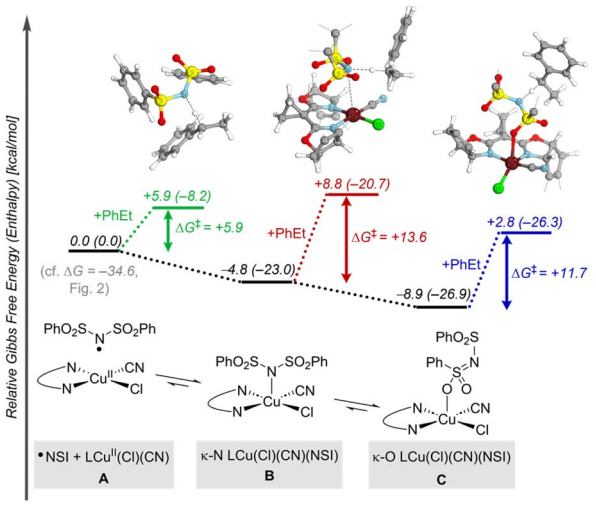

Fig. 3 Energy landscape for HAT in the reaction of $LCu^{II}(Cl)(CN)$, •NSI, and ethylbenzene. Gibbs free energies (enthalpies) [kcal mol^{-1}] are computed at 298.15 K at the M06-D3(0)/basis-II/SMD(CH_2Cl_2)//M06-D3(0)/basis-I level of theory.

activation free energies ($\Delta G^{\ddagger}$) for HAT from the 2° benzylic C–H bond in ethylbenzene were then computed for both of the isomeric Cu/NSI adducts as well as for free •NSI. Fig. 3 demonstrates that the HAT step involving free •NSI has a lower $\Delta G^{\ddagger}$ (+5.9 kcal mol^{-1}; green pathway) than the two Cu/NSI isomers (red and blue routes, with $\Delta G^{\ddagger}$ = +13.6 and +11.7 kcal mol^{-1} for the κ-N and κ-O isomers, respectively). However, the greater stability of the κ-O Cu/NSI adduct dictates that this species will be the resting state, and it provides access to the lowest overall transition-state energy for HAT.

To gain a better understanding of the HAT mechanism with •NSI and the κ-O Cu/NSI adduct, the relevant intrinsic bond orbitals (IBOs) were analyzed. IBOs are a set of localized molecular orbitals that represent exact molecular wave functions.[39] Analysis of the IBOs along the C–H reaction coordinate revealed that the HAT with free •NSI involves formal HAT between the carbon and nitrogen atoms, with synchronous transfer of electron and proton as a hydrogen atom. In contrast, the κ-O Cu/NSI species reacts *via* a proton-coupled electron transfer (PCET) pathway, whereby IBOs along the reaction coordinate reveal proton transfer to the proximal sulfonimide nitrogen and electron transfer from the alkylarene substrate to the lowest unoccupied molecular orbital (LUMO, $d_{x^2-y^2}$) of Cu (for details, see Section 10 of the ESI†).[40]

Experimental and computational comparison of HAT selectivities

Cu/NFSI-mediated C–H functionalization reactions appear to exhibit unique site-selectivity for benzylic C–H bonds. To gain insight into the reaction regioselectivity, we investigated HAT reactions of isobutylbenzene (**1**), isopentylbenzene (**2**) and 4-ethyltoluene (**3**) with κ-O Cu/NSI, *tert*-butoxyl radical (•O^{t}Bu) and chlorine radical (•Cl). Three synthetic methods in which these reactive species have been proposed as the HAT species include Cu/NFSI-catalyzed benzylic C–H methoxylation (κ-O Cu/NSI),[22] Ag/^{t}BuOCl-promoted C–H chlorination (•O^{t}Bu),[41] and SO_2Cl_2-mediated C–H chlorination (•Cl).[42]

The bond dissociation enthalpies (BDEs) of H–NSI, H–O^{t}Bu, and H–Cl were computed to be 107.0, 103.6 and 104.0 kcal mol^{-1}, respectively, indicating that all three reactive species have a strong thermodynamic driving force for HAT from the relevant C–H bonds. Experimental data indicate that the substrate C–H BDEs are as follows:[43] 3° aliphatic C–H bonds in **1** and **2**: 95.0 kcal mol^{-1}, the 1° benzylic C–H bonds in **3**: 90.0 kcal mol^{-1}, and the 2° benzylic C–H bonds in all three substrates: 87 kcal mol^{-1}. Computational BDEs for these substrates revealed similar values, with 2° benzylic C–H bonds generally showing lower values (85.2, 84.4, 83.5 kcal mol^{-1}, for **1**, **2**, and **3** respectively; see ESI, Table S8†) compared to the 3° aliphatic (91.8 and 92.6 kcal mol^{-1}, for **1** and **2**, respectively) and the 1° benzylic C–H bonds (87.3 kcal mol^{-1}, for **3**). This

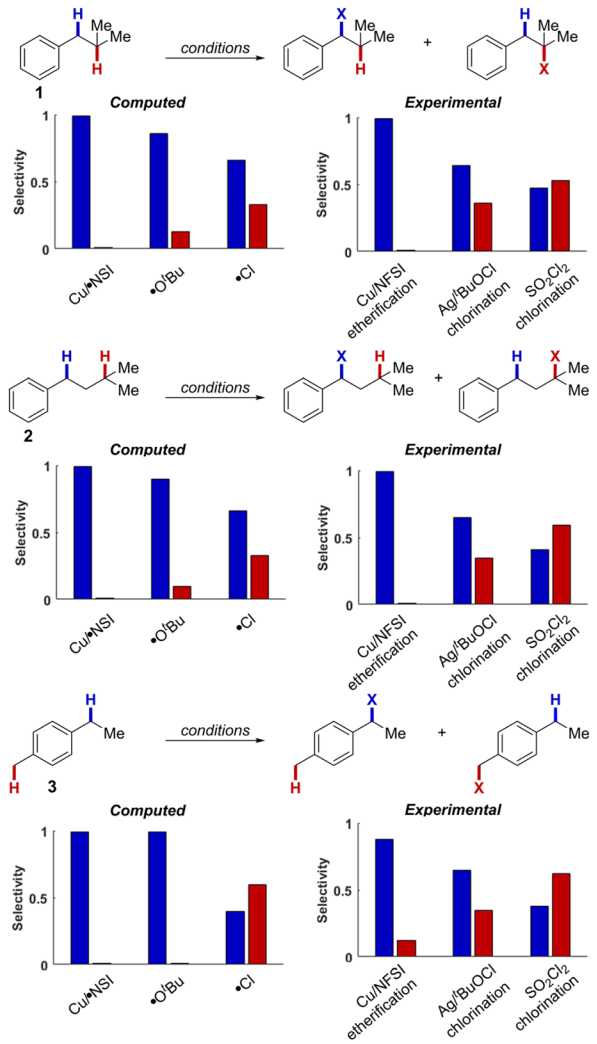

Fig. 4 Experimental selectivities compared against corresponding computational values derived from Gibbs free energies computed at 298.15 K at the M06-D3(0)/basis-II/SMD(CH_2Cl_2)//M06-D3(0)/basis-I level of theory.

distribution of C–H BDE values makes **1–3** an ideal set of compounds to interrogate site-selectivity.

We then evaluated the energy barriers for HAT ($\Delta G^{\ddagger}_{HAT}$) from the different C–H bonds in **1–3** to each of the reactive species: κ-O Cu/NSI, $^{\bullet}O^{t}Bu$, and $^{\bullet}Cl$ (see Section 12 in the ESI† for calculated thermodynamic and activation energies for each of the different HAT reactions). The $\Delta G^{\ddagger}_{HAT}$ values obtained with the κ-O Cu/NSI active species revealed that the activation energies for HAT from the 2° benzylic C–H bonds in **1** and **2** ($\Delta G^{\ddagger}_{b}$ = 10.9 and 10.1 kcal mol^{-1}, respectively; b = benzylic) are lower than those for the corresponding 3° aliphatic C–H bonds ($\Delta G^{\ddagger}_{a}$ = 15.7 and 15.5 kcal mol^{-1}; a = aliphatic). This preference for benzylic C–H activation ($\Delta\Delta G^{\ddagger}_{b-a} \sim 5$ kcal mol^{-1} for the 2° benzylic and 3° aliphatic C–H sites) aligns with the experimental observation of excellent benzylic site-selectivity in the reactions of **1** and **2** with Cu/NFSI (Fig. 4). Reactions of $^{\bullet}O^{t}Bu$ with **1** and **2** still favor HAT from the benzylic position but are calculated to be less selective, with $\Delta\Delta G^{\ddagger}_{b-a}$ values of only 1.1 and 1.3 kcal mol^{-1} for **1** and **2**, respectively. These energy differences correspond to 2° benzylic : 3° aliphatic C–H selectivities ranging from 6 : 1–9 : 1. In the reaction of **3**, which contains 1° and 2° benzylic C–H bonds, both κ-O Cu/NSI and $^{\bullet}O^{t}Bu$ are calculated to strongly favor reaction at the weaker 2° site ($\Delta\Delta G^{\ddagger}_{1°-2°} \sim 2.5$ kcal mol^{-1}). Reaction of the chlorine radical with both benzylic and 3° aliphatic sites is calculated to be barrierless,[44] and selectivity with this species simply reflects the statistical ratio of the corresponding C–H bonds in **1**, **2**, and **3**.

These DFT results were benchmarked with experimental analyses of the same substrates **1–3**, using the catalytic reaction systems proposed to involve the κ-O Cu/NSI,[22] $^{\bullet}O^{t}Bu$,[41] and $^{\bullet}Cl$[42] as the reactive species (Fig. 4, right charts). Under the Cu/NFSI and $SOCl_2$ reaction conditions, the experimental observations and computational predictions show strong agreement. Specifically, Cu/NFSI exhibits near-exclusive selectivity for reaction at the benzylic sites relative to the 3° aliphatic positions in **1** and **2** and high selectivity for 2° over 1° benzylic sites in **3**. Meanwhile, both experimental and computational analysis of the reactions involving $^{\bullet}Cl$ show poor selectivity with all three substrates, as significant reactivity is observed or predicted at both sites. Under the Ag/^{t}BuOCl conditions, the observed selectivity in the reactions with **1–3** is lower than that predicted for $^{\bullet}O^{t}Bu$, suggesting that the ^{t}BuOCl oxidant may generate other competent HAT species, such as $^{\bullet}Cl$, *in situ* that erode the selectivity. Overall, these data highlight the excellent site-selectivity accessible with the Cu/NSI species, which may be attributed to the interplay of two effects. Steric factors arising from the Cu–NSI adduct should favor reactivity at the 2° benzylic over the 3° aliphatic sites (see Fig. S15 of the ESI† for a representative steric map plot). In addition, the attenuated reactivity of the $^{\bullet}$NSI radical upon binding to Cu lowers the thermodynamic driving force for HAT, resulting in a later transition state that is more sensitive to the stability of the carbon-centered radical being formed.

Analysis of radical functionalization pathways

In Cu/NFSI reactions, the carbon-centred radical generated *via* HAT is proposed to undergo functionalization by a Cu^{II} species. Three different radical-functionalization pathways have been considered in these reactions, as depicted in Fig. 1C: (1) radical–polar crossover (RPC) with subsequent trapping of the resulting carbocation by a nucleophile, (2) radical addition to copper and reductive elimination from an organometallic copper intermediate, and (3) direct addition of the radical to a copper-bound nucleophile. Computational modelling techniques were used to examine the dependence of the various reaction pathways on the Cu coordination environment.

Experimental studies have shown that copper(I) and NFSI react rapidly in a 2 : 1 stoichiometry, upon mixing in organic solvent.[24] This reaction is expected to afford LCu^{II}(Cl)(F) and LCu^{II}(Cl)(NSI) as products (L = bis(oxazoline) ligand shown in

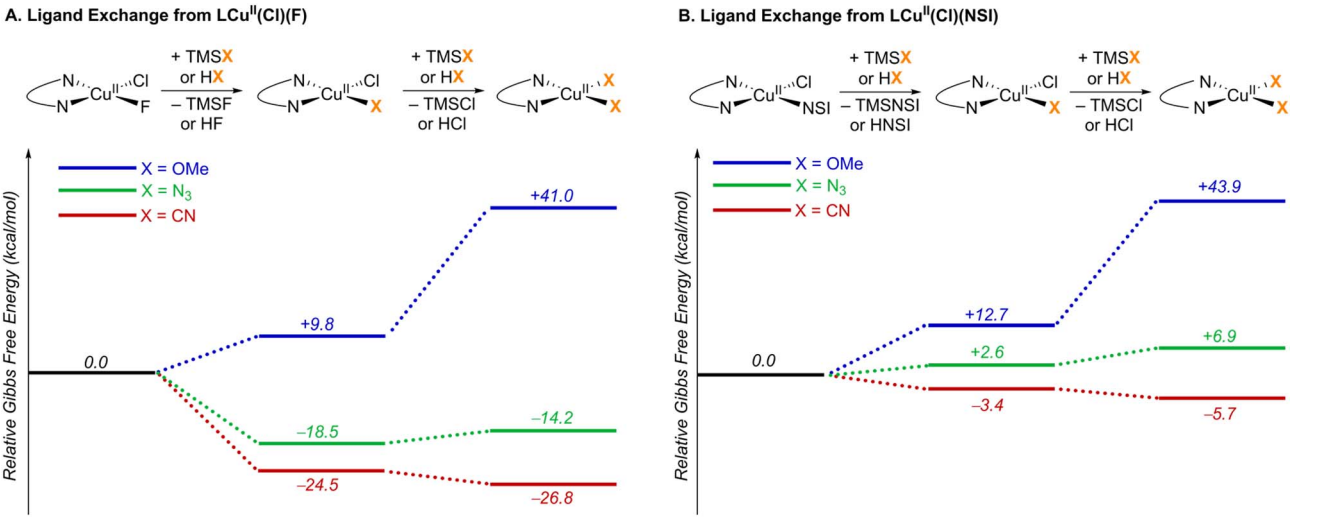

Fig. 5 Ligand exchange thermodynamics starting from two key Cu^{II} resting states: (A) LCu^{II}(Cl)(F) and (B) LCu^{II}(Cl)(NSI). L = bis(oxazoline) ligand shown in Fig. 2. Gibbs free energies (kcal mol^{-1}) are computed at 298.15 K at the M06-D3(0)/basis-II/SMD(CH_2Cl_2)//M06-D3(0)/basis-I level of theory.

Fig. 2), and these complexes served as the initial reference points for calculating the ligand-exchange energies shown in Fig. 5. The bis(sulfonimidyl) anion (NSI^-) is expected to be a rather weakly coordinating ligand; however, an X-ray crystal structure of $L'Cu^{II}(Cl)(NSI)$ (L' = bathophenanthroline) was obtained during the course of this study (see Section 2 of the ESI† for details). Relative energies were compared for the different $LCu^{II}(X)(Y)$ species that are relevant to cyanation, azidation, and methoxylation reactions (X, Y = Cl, F, NSI, CN, N_3, OMe; Fig. 5). A comprehensive tabulation of energies is provided in Table S5 of the ESI.†

TMS-substituted nucleophiles undergo highly exergonic ligand exchange with the fluoride of $LCu^{II}(Cl)(F)$, affording copper chloride/cyanide and chloride/azide complexes and TMSF (first step in Fig. 5A). Subsequent exchange of the chloride ligand with an azide is unfavourable ($\Delta G°$ = +4.3 kcal mol^{-1}), whereas exchange with a cyanide is favourable ($\Delta G° = -2.3$ kcal mol^{-1}). Cyanide also demonstrates favourable exchange with the anionic ligands in $LCu^{II}(Cl)(NSI)$ ($\Delta G° = -3.4$ and -2.3 kcal mol^{-1} for exchange with NSI and Cl ligands, respectively), whereas azide exchange is endergonic with this complex (Fig. 5B). Formation of a Cu–OMe species from the reaction of MeOH with either of these reference compounds is calculated to be very unfavourable ($\Delta G°$ = +9.8 – +43.9 kcal mol^{-1}), reflecting the weak basicity of the anionic ligands. Taken together, these results suggest that the most relevant Cu^{II} species for the different functionalization reactions consist of $LCu^{II}(CN)_2$ for cyanation, $LCu^{II}(Cl)(NSI)$ and $LCu^{II}(Cl)(N_3)$ for azidation, and $LCu^{II}(Cl)(NSI)$ and $LCu^{II}(Cl)(F)$ for methoxylation.

Subsequent calculations explored how the identity of the copper species influences the energetics of the different radical functionalization pathways (Fig. 6). RPC is initiated by one-electron oxidation of the benzylic radical by Cu^{II} to form a carbocation, which is then trapped by a nucleophile to afford a racemic coupling product. The energetics of electron transfer (ET) from the benzylic radical to the various $LCu^{II}(Cl)(X)$ species were calculated, and the reaction is endergonic in all cases (Fig. 6A; see Table S6 in the ESI†),[45] albeit only slightly uphill with $LCu^{II}(Cl)(NSI)$ ($\Delta G°_{ET} = +2.0$ kcal mol^{-1}), a Cu^{II} species expected to be present in the azidation and methoxylation reactions (*cf.* Fig. 5). Coordination of CN, N_3, and OMe nucleophiles to Cu^{II} in place of NSI lowers the $Cu^{II/I}$ redox potential relative to $LCu^{II}(Cl)(NSI)$ and increases the energy of ET, with $\Delta G°_{ET}$ values ranging from +8.4 to +21.8 kcal mol^{-1}.

Alternatively, the benzylic radical could react with the Cu^{II} species *via* addition, either at the Cu^{II} center (Fig. 6B) or at the coordinated ligand (Fig. 6C). Addition of the benzylic radical to the metal center is followed by rate-limiting reductive elimination (RE) to afford the coupling product. The computed activation free energies for the RE step reveal that the barriers are the lowest for the CN complexes (+8.9 – +9.4 kcal mol^{-1}), followed by N_3 (+14.7 kcal mol^{-1}) and OMe complexes (+16.0 kcal mol^{-1}) (Fig. 6B). In contrast, the energy barriers for radical addition to a Cu-bound ligand (RAL) in $LCu^{II}(Cl)(X)$ complexes are significantly lower and exhibit the opposite relative order: X = OMe ($\Delta G^{‡}_{RAL} = +0.8$ kcal mol^{-1}), N_3 ($\Delta G^{‡}_{RAL}$ = +2.7 kcal mol^{-1}), and CN ($\Delta G^{‡}_{RAL}$ = +4.4 – +4.7 kcal mol^{-1}) (Fig. 6C). The ditopic nature of the azide ligand complicates direct comparisons, since prior work has raised the possibility of both terminal and bridging Cu–azide complexes and radical addition to the proximal and distal N atom of the azide.[46] The favored pathway for the azide RAL pathway presented here corresponds to radical addition to the proximal *N*-atom (*i.e.*, coordinated to Cu), which resembles addition to the CN and OMe ligands.

The combined data from Fig. 5 and 6 allow a comparison of the inner- *versus* outer-sphere pathways for each of the different

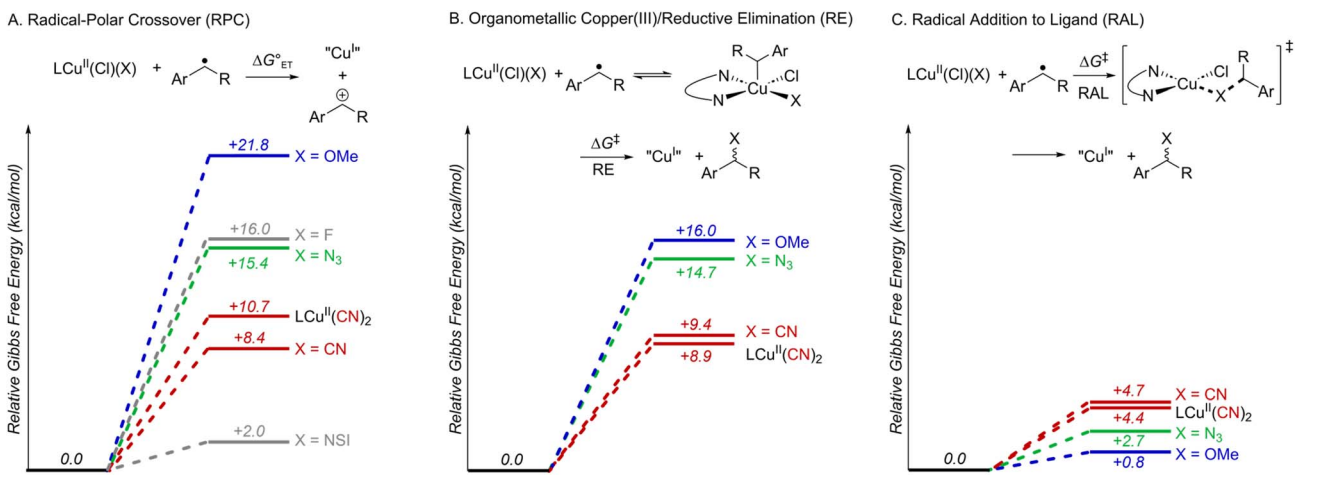

Fig. 6 Energetic trends for C–H functionalization *via* (A) radical–polar crossover, (B) organometallic Cu-mediated reductive elimination and (C) direct radical addition to ligands. Blue, green, and red lines correspond to methoxylation, azidation and cyanation reaction pathways, respectively. Grey lines in panel A represent RPC pathways with X = F and NSI ligands. The activation free energies ($\Delta G^{‡}$) for the RE and RAL pathways, shown in panels (B) and (C) respectively, are reported with reference to the energy of the spin–triplet precomplex of $LCu^{II}(Cl)(X)$ and PhCH(•)Me species set as the zero energy point. In all cases, Gibbs free energies (kcal mol^{-1}) are computed at 298.15 K at the M06-D3(0)/basis-II/SMD(CH_2Cl_2)//M06-D3(0)/basis-I level of theory.

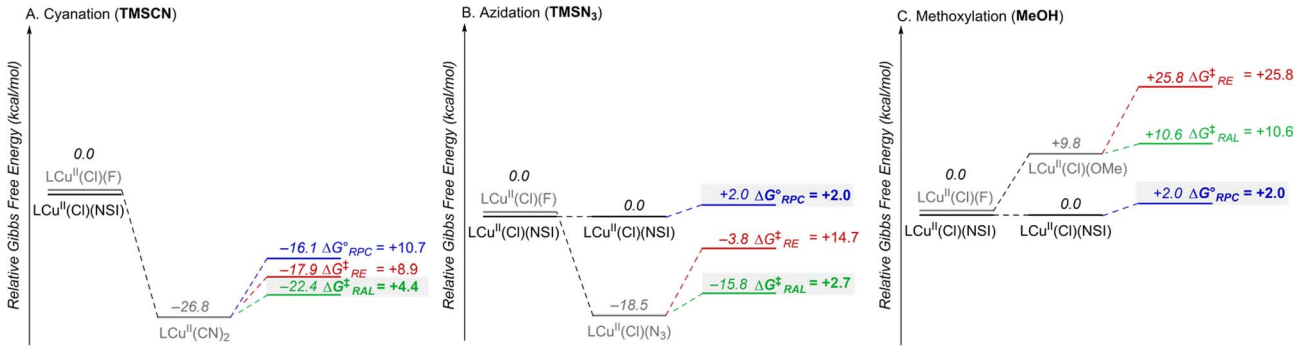

Fig. 7 Combination of the data in Fig. 5 and 6, showing the relative Gibbs free energies (kcal mol^{-1}) for the different Cu^{II} species and the mechanistic pathways (RPC, RE, RAL) for each of the three radical functionalization reactions, cyanation (A), azidation (B), and methoxylation (C). The RPC, RE and RAL pathways are depicted in blue, red, and green, respectively.

nucleophiles (Fig. 7). Favourable coordination of cyanide to copper generates Cu^{II}–CN species that are less oxidizing than LCu^{II}(Cl)(NSI) and support low-barrier inner-sphere pathways. The favoured pathway involves addition of a benzylic radical to the cyanide of the LCu^{II}(CN)$_2$ species (Fig. 7A). The initial report on this reactivity[17] proposed radical addition to Cu followed by reductive elimination, which also has a relatively low barrier ($\Delta G^{\ddagger}_{RE}$ = +8.9 kcal mol^{-1}). Both the RAL and RE mechanisms position the benzylic radical in close proximity to the chiral Cu centre and rationalize the high enantioselectivity observed experimentally (see Fig. S17 in the ESI† for a comparison between computed activation barriers for *R*- and *S*-isomers in RE and RAL pathways during cyanation of ethylbenzene). The less favourable coordination of azide and methoxide nucleophiles to Cu^{II}, relative to cyanide (*cf.* Fig. 5) will contribute to the presence of LCu^{II}(Cl)(NSI) in the azidation and methoxylation reaction mixtures. This relatively strong oxidant lowers the energy for electron transfer from the benzylic radical and favors the RPC pathway with N_3 and OMe nucleophiles (Fig. 7B and C). This conclusion is consistent with experimental data for these reactions, which generate racemic products, even when using chiral ligands.

Comparing different pathways for benzylic cation formation

The likely participation of the RPC pathway in some of these reactions highlights a relationship between these radical-relay reactions and other benzylic C–H functionalization reactions that proceed through benzylic cation intermediates. In the present reactions, the RPC mechanism arises from an HAT/ET sequence. Alternative pathways to access benzylic cations include concerted hydride transfer (H$^-$T), as in reactions with DDQ or other high-potential quinones,[31] or sequential ET/PT/ET, such as those involved in some photoredox reactions.[32] Results from these different approaches suggest that the HAT/ET reactions tolerate a wider range of benzylic substrates, not limited to those bearing electron-donating substituents. We sought to gain insights into this behaviour.

Computational studies were conducted to analyse the energetics of representative HAT/ET, H$^-$T, and ET/PT/ET reaction pathways using three different ethylbenzene derivatives, with –OMe, –H, and –Br groups as *para* substituents (Fig. 8). Analysis of the HAT step shows that the thermodynamics of HAT by the Cu/NSI species are highly favourable for all three substrates and largely unaffected by the para substituents (Fig. 8A). The kinetic barriers for the HAT steps are relatively low ($\Delta G^{\ddagger}$ = +5.2 – +12.4 kcal mol^{-1}) and show some electronic differentiation, with the lowest barrier evident for the electron-rich *p*-MeO derivative (TS-A, Fig. 8A): $\Delta\Delta G^{\ddagger}_{OMe/X} = 6.5$ and 7.2 kcal mol^{-1}, for the *p*-H and *p*-Br derivatives, respectively. Subsequent oxidation of the radical intermediates to the corresponding cations by LCu^{II}(Cl)(NSI) is affected by the *para* substitution of the substrate, although the impact of this sensitivity on reactivity is minimal because these ET steps are energetically less-demanding compared to the rate-limiting HAT steps. These observations explain why an HAT/ET method can accommodate a broad range of benzylic substrates. Trapping of the cations by the different nucleophiles to afford the coupling product is very exergonic in all cases (by >35 kcal mol^{-1}; Fig. S20†). Hydride transfer (H$^-$T) was investigated for the same series of ethylbenzene derivatives, using DDQ as the hydride acceptor.[47,48] The concerted H$^-$T steps to form the three carbocations show large kinetic barriers (Fig. 8B; TS-B, $\Delta G^{\ddagger}$ = +18.5 – +25.5 kcal mol^{-1}) compared to the HAT steps depicted in Fig. 8A. Moreover, formation of the cations is calculated to be endergonic (ΔG° = +5.7 – +17.6 kcal mol^{-1}), contrasting the energetically favorable HAT step. These features are consistent with experimental data showing that synthetically useful reactions with DDQ are mostly limited to electron-rich substrates.[31]

Finally, we analysed a photoredox method for benzylic C–H methoxylation reaction that uses an Ir-based photoredox catalyst ([Ir(dF(CF$_3$)ppy)$_2$(5,5′-dCF$_3$bpy)]PF$_6$; see Fig. S18†) and proceeds *via* an ET/PT/ET sequence (Fig. 8C).[32] Similar to the DDQ-promoted reactions, this method is primarily effective with electron-rich alkylarenes, such as those bearing *p*-OMe substituents. One-electron oxidation of the ethylbenzene derivatives considered here by triplet Ir^{III} complex (Ir^{III}*) yields the arene radical cation INT-C. For the *p*-OMe ethylbenzene derivative, this process is slightly exergonic ($\Delta G^{\circ}_{ET} = -0.7$ kcal mol^{-1}). The favourable nature of this initial ET step is expected to facilitate progression through the subsequent PT/ET steps, which are also

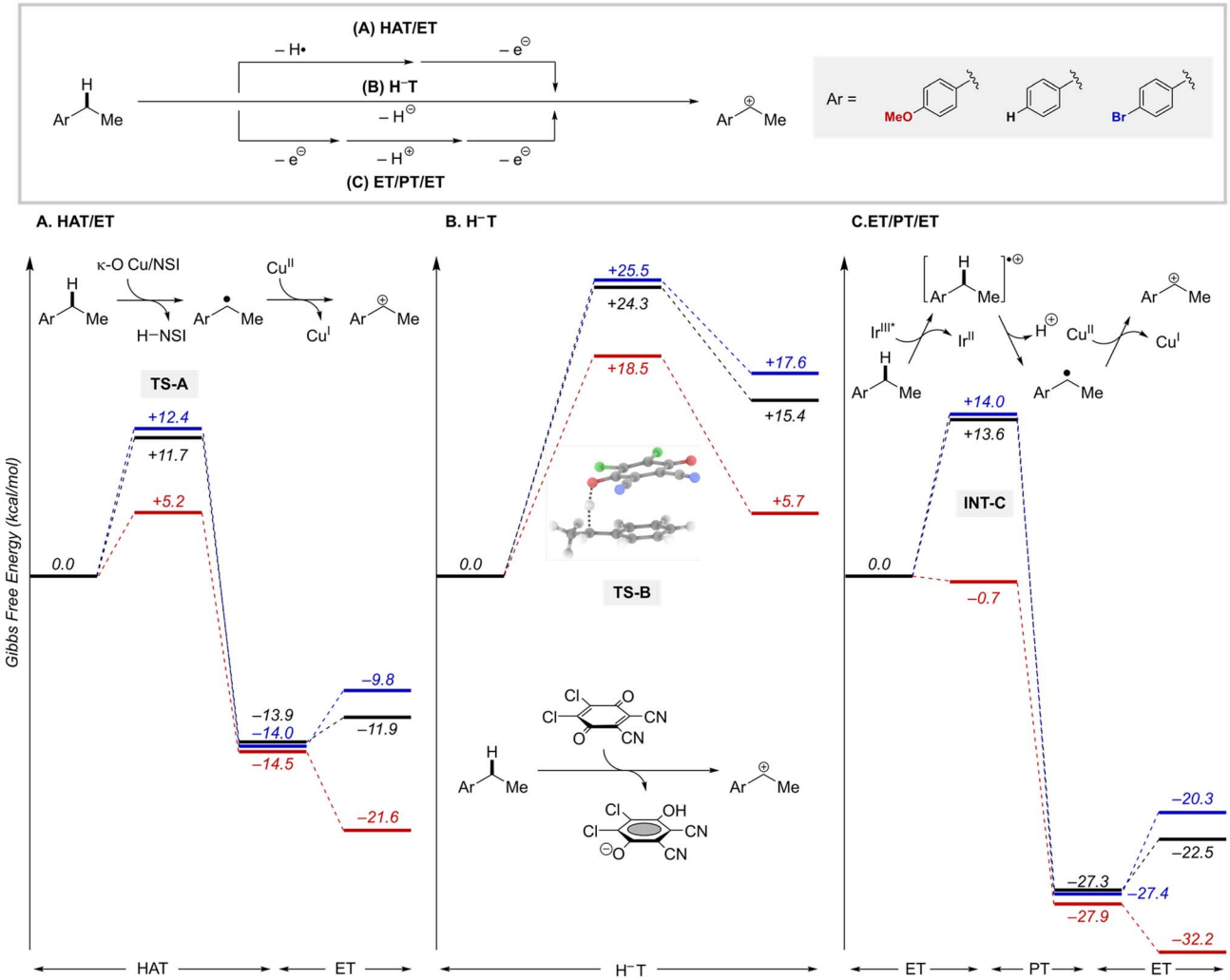

Fig. 8 Energy landscape for benzylic cation formation through (A) hydrogen-atom transfer/electron transfer (HAT/ET), (B) hydride transfer (H^-T), and (C) electron/proton/electron transfer (ET/PT/ET) *via* Ir^{III*}. Results for three *para* substituted benzylic substrates are shown in blue (*p*-Br), black (*p*-H) and red (*p*-OMe). Gibbs free energies are in kcal mol^{-1} computed at 298.15 K at the M06-D3(0)/basis-II/SMD(CH_2Cl_2)//M06-D3(0)/basis-I level of theory.

exergonic for the *p*-OMe derivative. In contrast, ET from the *p*-H and *p*-Br substrates by the same Ir^{III*} oxidant is thermodynamically unfavourable (ΔG° = +13.6 and 14.0 kcal mol^{-1}, respectively), suggesting that back-electron transfer from the reduced Ir complex to the radical cation could compete with deprotonation of the radical cation and hinder progression through the subsequent steps.

Overall, this analysis highlights important distinctions between benzylic C–H functionalization reactions that proceed *via* an HAT/ET pathway relative to those involving H^-T or ET/PT/ET pathways. The ability of HAT/ET methods to tolerate substrates spanning electron-rich to electron-deficient derivatives is not limited to the Cu/NFSI reactions evaluated here. Similar behavior is evident in a number of HAT-initiated photochemical reactions that proceed *via* an RPC pathway.[49] By comparison, H^-T and ET/PT/ET tend to show high selectivity for electron-rich substrates. This feature can be an advantage or disadvantage depending on the application.

Conclusions

The computational and experimental studies outlined herein clarify a series of important mechanistic features of Cu/NFSI-catalyzed benzylic C–H functionalization reactions, emphasizing the generation and functionalization of organic radicals. Full reaction coordinate analysis of benzylic C–H cyanation included an assessment of different HAT species that could react with benzylic C–H bonds. Analysis of these structures implicates a κ-O Cu/NSI adduct as the relevant HAT species and comparison of experimental data with a panel of different substrates across various HAT-mediated C–H functionalization methods highlight the unique benzylic site-selectivity accessed by Cu/NFSI relative to methods proposed to involve $^{\bullet}O^{t}Bu$ and $^{\bullet}Cl$ as the HAT reagent. The energetics of three different Cu^{II}-mediated radical functionalization pathways reveal that the preferred pathway can differ depending on the identity of the Cu^{II} species in the reaction mixture. For example, cyanide is

a good ligand for Cu^{II} and lowers the $Cu^{II/I}$ redox potential, disfavoring one-electron oxidation of the radical while supporting radical addition to the cyanide ligand of the Cu^{II}–CN intermediate. This inner-sphere radical-functionalization mechanism rationalizes the ability to achieve enantioselective cyanation of benzylic C–H bonds. For less coordinating azide and methoxide ligands, the data suggest that the oxidizing intermediate $LCu^{II}(Cl)(NSI)$ will be present in the reaction manifold and that this species can promote outer-sphere oxidation of benzylic radicals to generate benzylic cations. This radical–polar crossover pathway involving stepwise HAT/ET has been compared to two alternative C–H functionalization mechanisms that generate benzylic cation intermediates, H^-T and ET/PT/ET. The results rationalize why the HAT/ET sequence accesses a broader C–H substrate scope relative to the other methods. Thus, while the radical–polar crossover mechanism is not compatible with enantioselective bond formation, the HAT/ET sequence presents an advantageous strategy to access reactive benzylic cations. The collective insights gained from this study provide a valuable foundation for future studies, targeting unmet challenges, such as expanding the scope of enantioselective transformation, achieving site-selective functionalization of less-activated C–H bonds, and diversifying reactivity to include heterobenzylic C–H sites.

Data availability

The data supporting this article have been included as part of the ESI,† including, experimental selectivity studies, energies of all computed structures, IBO transformations in PDF format, and Cartesian coordinates of DFT-calculated structures in XYZ format. Crystallographic data for compounds have been deposited at the Cambridge Crystallographic Data Centre (CCDC) under access number 2239614.

Author contributions

M. M. and J. A. B. contributed equally to this work. The manuscript was written through contributions of all authors.

Conflicts of interest

There are no conflicts to declare.

Acknowledgements

We thank Amelia Wheaton for assistance with X-ray crystallography, and Austin Bleskacek for help with editing the manuscript. Funding for this work was provided by the NIH (R35 GM134929 to S. S. S), a Ruth L. Kirschstein NRSA fellowship to J. A. B. (F32 GM129909), a doctoral dissertation fellowship from the University of Minnesota (M. M.), and postdoctoral support from the Alexander von Humboldt Foundation (M. M). Spectroscopic instrumentation was partially supported by the NIH (S10 OD020022) and the NSF (CHE-1048642).

Notes and references

1 K. R. Campos, P. J. Coleman, J. C. Alvarez, S. D. Dreher, R. M. Garbaccio, N. K. Terrett, R. D. Tillyer, M. D. Truppo and E. R. Parmee, *Science*, 2019, **363**, eaat0805.
2 T. Cernak, K. D. Dykstra, S. Tyagarajan, P. Vachal and S. W. Krska, *Chem. Soc. Rev.*, 2016, **45**, 546–576.
3 D. C. Blakemore, L. Castro, I. Churcher, D. C. Rees, A. W. Thomas, D. M. Wilson and A. Wood, *Nat. Chem.*, 2018, **10**, 383–394.
4 J. Wencel-Delord and F. Glorius, *Nat. Chem.*, 2013, **5**, 369–375.
5 D. L. Golden, S.-E. Suh and S. S. Stahl, *Nat. Rev. Chem*, 2022, **6**, 405–427.
6 Z. Zhang, P. Chen and G. Liu, *Chem. Soc. Rev.*, 2022, **51**, 1640–1658.
7 M. Kharasch and A. Fono, *J. Org. Chem.*, 1958, **23**, 325–326.
8 M. S. Kharasch and G. Sosnovsky, *J. Am. Chem. Soc.*, 1958, **80**, 756.
9 J. K. Kochi, *J. Am. Chem. Soc.*, 1962, **84**, 774–784.
10 R. T. Gephart, C. L. McMullin, N. G. Sapiezynski, E. S. Jang, M. J. Aguila, T. R. Cundari and T. H. Warren, *J. Am. Chem. Soc.*, 2012, **134**, 17350–17353.
11 B. L. Tran, M. Driess and J. F. Hartwig, *J. Am. Chem. Soc.*, 2014, **136**, 17292–17301.
12 E. S. Jang, C. L. McMullin, M. Käß, K. Meyer, T. R. Cundari and T. H. Warren, *J. Am. Chem. Soc.*, 2014, **136**, 10930–10940.
13 B. L. Tran, B. Li, M. Driess and J. F. Hartwig, *J. Am. Chem. Soc.*, 2014, **136**, 2555–2563.
14 A. Vasilopoulos, S. L. Zultanski and S. S. Stahl, *J. Am. Chem. Soc.*, 2017, **139**, 7705–7708.
15 For related studies on C–H fluorination, see: (*a*) C. R. Pitts, S. Bloom, R. Woltornist, D. J. Auvenshine, L. R. Ryzhkov, M. A. Siegler and T. Lectka, *J. Am. Chem. Soc.*, 2014, **136**, 9780–9791; (*b*) C. R. Pitts, B. Ling, J. A. Snyder, A. E. Bragg and T. Lectka, *J. Am. Chem. Soc.*, 2016, **138**, 6598–6609; (*c*) J. B. Roque, R. Sarpong and D. G. Musaev, *J. Am. Chem. Soc.*, 2021, **143**, 3889–3900; (*d*) Z. Liu, H. Chen, Y. Lv, X. Tan, H. Shen, H.-Z. Yu and C. Li, *J. Am. Chem. Soc.*, 2018, **140**, 6169–6175.
16 Z. Ni, Q. Zhang, T. Xiong, Y. Zheng, Y. Li, H. Zhang, J. Zhang and Q. Liu, *Angew. Chem., Int. Ed.*, 2011, **51**, 1244–1247.
17 W. Zhang, F. Wang, S. D. McCann, D. Wang, P. Chen, S. S. Stahl and G. Liu, *Science*, 2016, **353**, 1014–1018.
18 W. Zhang, P. Chen and G. Liu, *J. Am. Chem. Soc.*, 2017, **139**, 7709–7712.
19 W. Zhang, L. Wu, P. Chen and G. Liu, *Angew. Chem., Int. Ed.*, 2019, **58**, 6425–6429.
20 H. Xiao, Z. Liu, H. Shen, B. Zhang, L. Zhu and C. Li, *Chem*, 2019, **5**, 940–949.
21 J. Li, Z. Zhang, L. Wu, W. Zhang, P. Chen, Z. Lin and G. Liu, *Nature*, 2019, **574**, 516–521.
22 H. Hu, S.-J. Chen, M. Mandal, S. M. Pratik, J. A. Buss, S. W. Krska, C. J. Cramer and S. S. Stahl, *Nat. Catal.*, 2020, **3**, 358–367.

23 A. Vasilopoulos, D. L. Golden, J. A. Buss and S. S. Stahl, *Org. Lett.*, 2020, **22**, 5753–5757.
24 J. A. Buss, A. Vasilopoulos, D. L. Golden and S. S. Stahl, *Org. Lett.*, 2020, **22**, 5749–5752.
25 L. Fu, Z. Zhang, P. Chen, Z. Lin and G. Liu, *J. Am. Chem. Soc.*, 2020, **142**, 12493–12500.
26 S. Liu, R. Achou, C. Boulanger, G. Pawar, N. Kumar, J. Lusseau, F. Robert and Y. Landais, *Chem. Commun.*, 2020, **56**, 13013–13016.
27 S.-E. Suh, L. E. Nkulu, S. Lin, S. W. Krska and S. S. Stahl, *Chem. Sci.*, 2021, **12**, 10380–10387.
28 C. Jiang, P. Chen and G. Liu, *CCS Chem.*, 2021, **3**, 1884–1893.
29 S.-J. Chen, D. L. Golden, S. W. Krska and S. S. Stahl, *J. Am. Chem. Soc.*, 2021, **143**, 14438–14444.
30 M. A. Lopez, J. A. Buss and S. S. Stahl, *Org. Lett.*, 2021, **24**, 597–601.
31 (*a*) C. Song, X. Dong, H. Yi, C.-W. Chiang and A. Lei, *ACS Catal.*, 2018, **8**, 2195–2199; (*b*) C. A. Morales-Rivera, P. E. Floreancig and P. Liu, *J. Am. Chem. Soc.*, 2017, **139**, 17935–17944.
32 B. J. Lee, K. S. DeGlopper and T. P. Yoon, *Angew. Chem., Int. Ed.*, 2019, **59**, 197–202.
33 Y. Zhao and D. G. Truhlar, *Theor. Chem. Acc.*, 2007, **120**, 215–241.
34 S. Grimme, S. Ehrlich and L. Goerigk, *J. Comput. Chem.*, 2011, **32**, 1456–1465.
35 A. V. Marenich, C. J. Cramer and D. G. Truhlar, *J. Phys. Chem. B*, 2009, **113**, 6378–6396.
36 (*a*) F. Weigend and R. Ahlrichs, *Phys. Chem. Chem. Phys.*, 2005, **7**, 3297–3305; (*b*) B. P. Pritchard, D. Altarawy, B. Didier, T. D. Gibson and T. L. Windus, *J. Chem. Inf. Model.*, 2019, **59**, 4814–4820.
37 (*a*) H. Zhang, Y. Song, J. Zhao, J. Zhang and Q. Zhang, *Angew. Chem., Int. Ed.*, 2014, **53**, 11079; (*b*) B. E. Haines, T. Kawakami, K. Kuwata, K. Murakami, K. Itami and D. G. Musaev, *Chem. Sci.*, 2017, **8**, 988–1001.
38 Si–F BDE in TMS–F is ∼160.0 kcal mol^{-1}; see, for instance, Y.-R. Luo, *Comprehensive Handbook of Chemical Bond Energies*, CRC Press, Boca Raton, FL, 1st edn, 2007, DOI: 10.1201/9781420007282.
39 (*a*) G. Knizia, *J. Chem. Theory Comput.*, 2013, **9**, 4834–4843; (*b*) J. E. Klein and G. Knizia, *Angew. Chem., Int. Ed.*, 2018, **57**, 11913–11917.
40 (*a*) M. Mandal, C. E. Elwell, C. J. Bouchey, T. J. Zerk, W. B. Tolman and C. J. Cramer, *J. Am. Chem. Soc.*, 2019, **141**, 17236–17244; (*b*) C. E. Elwell, M. Mandal, C. J. Bouchey, L. Que, C. J. Cramer and W. B. Tolman, *Inorg. Chem.*, 2019, **58**, 15872–15879; (*c*) M. Mandal, C. J. Cramer, D. G. Truhlar, J. Sauer and L. Gagliardi, *ACS Catal.*, 2020, **10**, 10051–10059.
41 J. Ozawa and M. Kanai, *Org. Lett.*, 2017, **19**, 1430–1433.
42 M. S. Kharasch and H. C. Brown, *J. Am. Chem. Soc.*, 1939, **61**, 2142–2150.
43 (*a*) E. N. Bess, R. J. DeLuca, D. J. Tindall, M. S. Oderinde, J. L. Roizen, J. Du Bois and M. S. Sigman, *J. Am. Chem. Soc.*, 2014, **136**, 5783–5789; (*b*) E. N. Bess, D. M. Guptill, H. M. Davies and M. S. Sigman, *Chem. Sci.*, 2015, **6**, 3057–3062.
44 (*a*) B. Giese and J. Meixner, *Angew Chem. Int. Ed. Engl.*, 1979, **18**, 154–155; (*b*) A. A. Scala, *J. Chem. Educ.*, 2004, **81**, 1661–1664.
45 We chose not to estimate electron transfer (ET) barriers due to uncertainties in calculating reorganization energies and other factors influencing ET rates, like solvent properties and the driving force for ET. Without precise estimates of these parameters, predicting ET rates with Marcus theory would be speculative. The thermodynamic change in the radical–polar crossover step serves as a lower bound for the ET barrier.
46 S.-E. Suh, S.-J. Chen, M. Mandal, I. A. Guzei, C. J. Cramer and S. S. Stahl, *J. Am. Chem. Soc.*, 2020, **142**, 11388–11393.
47 D. J. Maloney, S. Chen and S. M. Hecht, *Org. Lett.*, 2006, **8**, 1925–1927.
48 L. M. Chapman, J. C. Beck, L. Wu and S. E. Reisman, *J. Am. Chem. Soc.*, 2016, **138**, 9803–9806.
49 (*a*) G. Pandey and R. Laha, *Angew. Chem., Int. Ed.*, 2015, **54**, 14875–14879; (*b*) G.-X. Li, C. A. Morales-Rivera, F. Gao, Y. Wang, G. He, P. Liu and G. Chen, *Chem. Sci.*, 2017, **8**, 7180–7185; (*c*) I. N.-M. Leibler, M. A. Tekle-Smith and A. G. Doyle, *Nat. Commun.*, 2021, **12**, 6950; (*d*) Y. Zhang, N. A. Fitzpatrick, M. Das, I. P. Bedre, H. G. Yayla, M. S. Lall and P. Z. Musacchio, *Chem Catal.*, 2022, **2**, 292–308; (*e*) M. Das, L. Zamani, C. Bratcher and P. Z. Musacchio, *J. Am. Chem. Soc.*, 2023, **145**, 3861–3868.
50 M. J. Frisch, G. W. Trucks, H. B. Schlegel. G. E. Scuseria, M. A. Robb, *et al.*, *Gaussian 16, Revision B.01*, Gaussian, Inc., Wallingford, CT, 2016.
51 (*a*) B. Dereli, M. A. Ortuño and C. J. Cramer, *ChemPhysChem*, 2018, **19**, 959–966; (*b*) T. Malcomson, P. Repiščák, S. Erhardt and M. J. Paterson, *ACS Omega*, 2022, **7**, 45057–45066.
52 (*a*) K. Yamaguchi, Y. Takahara and T. Fueno, in *Applied Quantum Chemistry*, ed. V. H. Smith, H. F. Schaefer, and K. Morokuma, Springer Netherlands, Dordrecht, 1986, pp. 155–184; (*b*) Y. Kitagawa, K. Saito, and K. Yamaguchi, in *Symmetry (Group Theory) and Mathematical Treatment in Chemistry*, ed. T. Saito, IntechOpen, Rijeka, 2018, ch. 7, pp. 121–139.
53 F. Neese, F. Wennmohs, U. Becker and C. Riplinger, *J. Chem. Phys.*, 2020, **152**, 224108.
54 (*a*) G. Knizia and J. E. M. N. Klein, *Angew. Chem., Int. Ed.*, 2015, **54**, 5518–5522; (*b*) G. Knizia, **http://www.iboview.org/**, accessed on July 10, 2022.